Received: 23 May 2017 | Revised: 19 January 2018 | Accepted: 19 March 2018

DOI: 10.1002/stc.2187

RESEARCH ARTICLE

WILEY

Sensing dynamic displacements in masonry rail bridges using 2D digital image correlation

Sinan Acikgoz[1,2] | Matthew J. DeJong[3] | Kenichi Soga[4]

[1]Centre for Smart Infrastructure and Construction, University of Cambridge, Cambridge, UK

[2]Department of Engineering Science, University of Oxford, 17 Parks Road, OX1 3PJ Oxford, UK

[3]Department of Engineering, University of Cambridge, Cambridge, UK

[4]University of California, Berkeley, California, USA

Correspondence
Sinan Acikgoz, Department of Engineering Science, University of Oxford, 17 Parks Road, OX1 3PJ, Oxford.
Email: sinan.acikgoz@eng.ox.ac.uk

Funding information
Innovate UK, Grant/Award Number: EP/L010917/1; EPSRC, Grant/Award Number: EP/L010917/1

Summary

Dynamic displacement measurements provide useful information for the assessment of masonry rail bridges, which constitute a significant part of the bridge stock in the United Kingdom and Europe. Commercial 2D digital image correlation (DIC) techniques are well suited for this purpose. These systems provide precise noncontact displacement measurements simultaneously at many locations of the bridge with an easily configured camera set-up. However, various sources of errors can affect the resolution, repeatability, and accuracy of DIC field measurements. Typically, these errors are application specific and are not automatically corrected by commercial software. To address this limitation, this paper presents a survey of relevant DIC errors and discusses methods to minimise the influence of these errors during equipment set-up and data processing. A case study application of DIC for multipoint displacement measurement of a masonry viaduct in Leeds is then described, where potential errors due to lighting changes, image texture, and camera movements are minimised with an appropriate set-up. Pixel-metric scaling errors are kept to a minimum with the use of a calibration method, which utilises vanishing points in the image. However, comparisons of DIC relative displacement measurements to complementary strain measurements from the bridge demonstrate that other errors may have significant influence on the DIC measurement accuracy. Therefore, the influence of measurement errors due to lens radial distortion and out-of-plane movements is quantified theoretically with pinhole camera and division distortion models. A method to correct for errors due to potential out-of-plane movements is then proposed.

KEYWORDS

digital image correlation, field testing and monitoring, masonry arch bridge, measurement error, out-of-plane movement, pinhole camera

1 | INTRODUCTION

According to a recent survey, there are approximately 18,000 masonry rail bridges in the United Kingdom, and this corresponds to 47% of the rail bridge stock. Most of the existing masonry bridges date back to the 19th century and have

been in continued use since then. Remarkably, the majority of the masonry bridge stock remains in good condition. However, around 10% of these bridges are assessed to be in poor condition and are showing signs of accelerated deterioration.[1]

Dynamic rail loading is one of the main contributors to deterioration.[2] The increases observed in the weight, length, and speed of modern trains have resulted in more onerous loading demands, which have caused damage in masonry bridge structures or foundations. Cyclic loading of damaged areas causes further deterioration, accelerating the degradation of materials due to ageing and water ingress.[3]

In the United Kingdom, the bridges that are vulnerable to their train route loading demands are determined through codified structural analyses and visual inspections.[4] Typically, a yearly visual assessment is carried out to keep track of degradation in these bridges. A more detailed assessment is carried out every 6 years, to manually measure the size and extent of existing cracks on the structure and determine water damage and ring separation through hammer tapping (e.g., see other works[5,6]).

Monitoring of the structure is sometimes specified when the bridge experiences (or is expected to experience) accelerated deterioration. To investigate the bridge response, periodic displacement measurements are taken using displacement gauges (with devices such as linear variable displacement transformers) mounted on poles and fixed on the ground. Typically vertical crown displacement is measured with a high sampling rate and a measurement accuracy of 0.01 mm.[7–9] Although this measurement technique is precise and easy to set-up, it requires inconvenient (and sometimes unfeasible) access requirements to the underside of the bridge. Although several deflection poles can be connected to a data logger to get simultaneous measurements and obtain more comprehensive data, in practice, only one deflection pole is typically used to measure crown vertical deflections, which may not be critical.

Alternative noncontact measurement techniques, such as laser vibrometry, microwave radar interferometry, and digital image correlation (DIC), allow precise dynamic measurement of structures without requiring road closure or access to the structure.[10–12] However, similar to linear variable displacement transformers, laser vibrometry equipment can only measure the position of a single target. Microwave radar interferometry does not have this limitation and can measure multiple targets within a radar image. However, displacements are measured only along the line of sight of the instrument. In contrast, the DIC sensing technique allows planar displacement measurement of multiple targets in its field of view. This technique uses video cameras, which record images of the viaduct from a distance at a high sampling rate. By comparing recorded images, DIC algorithms determine the movement of small targets in the image by subpixel correlation, allowing precise measurement of displacements. Under ideal conditions, the DIC system can achieve similar measurement accuracy (0.01 mm) to conventional displacement gauges.

Owing to their aforementioned sensing capabilities, the use of DIC systems is increasing in popularity for monitoring civil engineering structures.[13] This is facilitated by the availability of commercial DIC systems, such as the Imetrum's Dynamic Monitoring Station (DMS) system used in this study, which capture precise displacements with an easily configured camera set-up. However, errors from different sources can significantly affect DIC measurement resolution, repeatability, and accuracy.[12] Many of these errors are application specific and are not automatically corrected by commercial software. Therefore, operators and analysts of these commercial systems need to understand the potential sources of errors and minimise their influence during field deployment and data processing. The objective of this paper is to identify relevant sources of DIC measurement errors for monitoring masonry viaducts and propose methods to minimise/compensate for these errors.

The paper is structured as follows. The DIC technique is introduced in Section 2, and relevant measurement errors for monitoring masonry viaducts with the DIC technique are surveyed in Section 3. Following this, an application of DIC to a masonry viaduct is discussed in Section 4. By using complementary field measurements, the resolution, repeatability, and accuracy of the DIC system are determined in Section 5. In Section 6, a theoretical discussion of critical errors in the DIC system leads to the development of postprocessing methods to correct for them. Finally, Section 7 summarises conclusions from this study.

2 | 2D DIC

DIC was largely developed in the 1980s, and it is well established today as a displacement measurement technique.[12] It is extensively used in the field of civil engineering for laboratory investigations involving static loading (e.g., White et al.[14]), although a number of field investigations (some of them involving dynamic loading) have also been reported.[15–20]

In 2D DIC, which will be examined in this paper (see Figure 1), a single camera is positioned to have the desired object plane in its field of view. In laboratory conditions, the camera sensor (i.e., image plane) can be placed parallel to the object plane. However, when monitoring structures in the field, parallel placement may not be possible or desirable. In this case, a general pinhole camera model can be used to describe the projection of a target in the object plane to the image plane with the following equation:

$$s\begin{bmatrix} u \\ v \\ 1 \end{bmatrix} = \mathbf{K}\left(\mathbf{R}\begin{bmatrix} X \\ Y \\ Z \end{bmatrix} + \mathbf{T}\right), \tag{1}$$

where the homogenous coordinates of the target reflection in the image plane are given as $[u, v, 1]^{\mathrm{T}}$ and the world coordinates of the target located in the object plane are given as $[X, Y, Z]^{\mathrm{T}}$. In addition, the rotation matrix $\mathbf{R}$ and the translation vector $\mathbf{T}$ transform the *XYZ* world coordinate system into the metric camera coordinate system, whereas the intrinsic camera matrix $\mathbf{K}$ and the scale factor s transform the results into the image plane with the *UV* pixel coordinate system. For nonparallel image and object planes, the scale factor s depends on the position of the target in the object plane. Note that the origin of the *UV* coordinate system is located on the bottom right of the camera sensor (see Figure 1a).

If the object surface features sufficient pixels and has enough contrast, DIC algorithms can track the movement of a small target (called target C, with pixel coordinates $[u_C, v_C, 1]^{\mathrm{T}}$) in the image. This can be done by fitting a zeroth-order shape function to the cross-correlation results of two image frames taken at different times. The peak of the fitted function is used to determine the new location of the target after rigid body in-plane translation (denoted by C' with coordinates $[u_{C'}, v_{C'}, 1]^{\mathrm{T}}$) with subpixel resolution. More advanced shape functions can also consider in-plane elastic deformation and rigid body rotation of the target (see the illustration in Figure 1b and Murray et al.[21]). Once the deformations are determined in the image plane with pixel units, it is necessary to convert these into metric units. Because 2D DIC only measures movements of the target in the object plane, metric displacements are described by ΔX_C and ΔY_C whereas out-of-plane movements, denoted by ΔZ_C, are assumed to be zero. Finding the ΔX_C and ΔY_C movements requires solving the following equation, which is obtained from Equation (1):

$$\begin{bmatrix} \Delta X_c \\ \Delta Y_c \\ 0 \end{bmatrix} = \mathbf{R}^{-1}\mathbf{K}^{-1}\left(s_{C'}\begin{bmatrix} u_{C'} \\ v_{C'} \\ 1 \end{bmatrix} - s_C\begin{bmatrix} u_C \\ v_C \\ 1 \end{bmatrix}\right). \tag{2}$$

Solving Equation (2) for the displacements ΔX_C and ΔY_C requires knowledge of the matrices $\mathbf{K}$ and $\mathbf{R}$ as well as the scale factors $s_{C'}$ and s_C, which describe the scale factors for deformed and undeformed positions of the target C. The intrinsic camera matrix $\mathbf{K}$ can be estimated from manufacturer specifications concerning lens focal length f (expressed

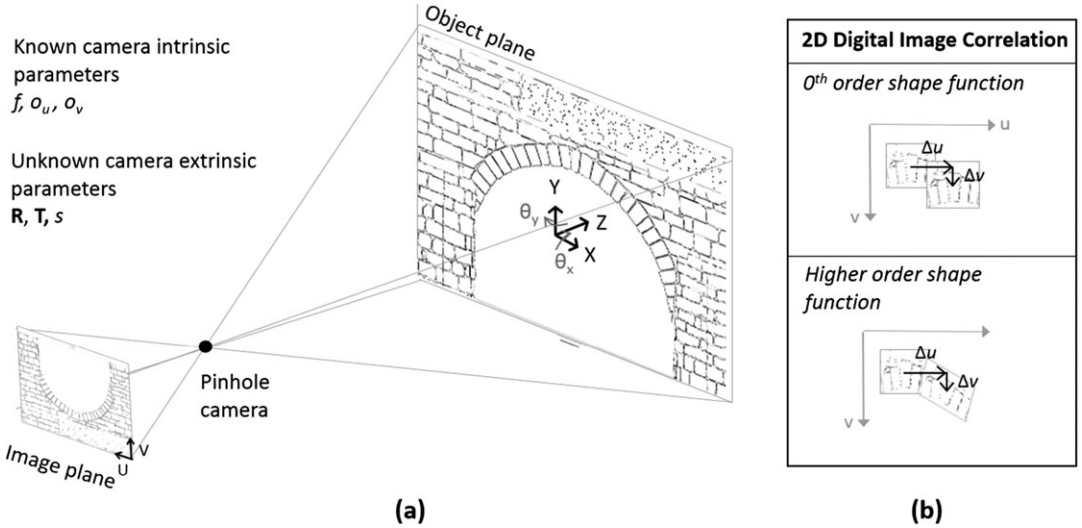

FIGURE 1 A schematic illustrating the various components and parameters of the 2D digital image correlation technique

in metric units), principal point (o_u, o_v) (in pixel units), and a skew coefficient. For an industrial grade camera, the principal point can be assumed to be located on the centre of the image and the skew coefficient is typically negligible. The focal length can also be expressed in pixel units when multiplied by the magnification factor $\alpha = H_{pixel}/H_{sensor}$, where H_{pixel} and H_{sensor} denote horizontal pixel and metric size of the image sensor. Using these parameters, $\mathbf{K}$ is defined as follows:

$$\mathbf{K} = \begin{bmatrix} \alpha f & 0 & o_u \\ 0 & -\alpha f & o_v \\ 0 & 0 & 1 \end{bmatrix}. \tag{3}$$

Unknown camera extrinsic parameters $\mathbf{R}$ and s_C are required to relate the pixel movements to metric displacements (see Equation (2)). When the object and image planes are parallel, the rotation matrix becomes an identity matrix, and only a single distance between two targets in the object plane is necessary for calibration. In this case, $s_{C'} = s_C$. This type of calibration is commonly called scaling factor calibration. Due to its apparent simplicity, scaling factor calibration has been used in numerous DIC monitoring studies carried out in the field, even when the object and image planes are not parallel (e.g., Hoag et al.[19] and Khuc and Catbas[22]). However, this approach can introduce notable errors, as the assumption of parallel image and object planes for a nonorthographic set-up results in out-of-plane movements, which can reduce measurement accuracy significantly (see Section 7).

To avoid potential errors in set-ups involving nonparallel object and image planes, it is essential to capture camera extrinsic parameters. These parameters are typically identified through on-site calibration by specifying the world coordinates (X, Y, and Z) of a minimum of four targets in the object plane.[23] However, this calibration method is prone to errors, because it requires precise measurement of the coordinates of multiple targets with respect to a fixed coordinate frame. Even when measurement of multiple targets is possible (i.e., with a laser scanner), identifying identical targets in a laser scan and an image frame may be challenging.

In an alternative and more efficient approach, only a single object coordinate is necessary for calibration. To do this, it is necessary to identify the rotation matrix by other means. Two vanishing points in the image can be used to identify the relative rotation of the world coordinate system with respect to the camera coordinate system.[23–25] For each axis in the world coordinate system, a vanishing point can be determined from two lines parallel to the considered axis. For instance, the pixel location of the vanishing points of the Y and Z axes $[u_{vpY}, v_{vpY}, 1]^{\mathrm{T}}$ and $[u_{vpZ}, v_{vpZ}, 1]^{\mathrm{T}}$ can be related to the rotation matrix via the following relations:

$$\mathbf{r}_2 = \frac{\mathbf{K}^{-1}\begin{bmatrix} u_{vpY} \\ v_{vpY} \\ 1 \end{bmatrix}}{\left\| \mathbf{K}^{-1}\begin{bmatrix} u_{vpY} \\ v_{vpY} \\ 1 \end{bmatrix} \right\|}, \mathbf{r}_3 = \frac{\mathbf{K}^{-1}\begin{bmatrix} u_{vpZ} \\ v_{vpZ} \\ 1 \end{bmatrix}}{\left\| \mathbf{K}^{-1}\begin{bmatrix} u_{vpZ} \\ v_{vpZ} \\ 1 \end{bmatrix} \right\|}, \mathbf{R} = [\mathbf{r}_2 \times \mathbf{r}_3, \mathbf{r}_2, \mathbf{r}_3], \tag{4}$$

where the operators $\|\|$ and $\times$ denote the norm of the vector and cross product operations and $\mathbf{r}_j$ describes the jth column of the rotation matrix $\mathbf{R}$. Once the rotation matrix is determined, the relative pitch, yaw, and roll angles between the camera and world coordinate systems (denoted by $\delta\theta_X$, $\delta\theta_Y$, $\delta\theta_Z$, respectively) can be calculated.

After determining the rotation matrix $\mathbf{R}$ using vanishing points, the scale factor s_C needs to be determined to relate pixel movements to metric movements using Equation (2). For a given target C, s_C can be determined from Equation (1), by specifying its world coordinates $[X_C, Y_C, Z_C]^{\mathrm{T}}$. These world coordinates can be retrieved from a laser scan survey of the structure. After aligning the bridge transverse axis of the point cloud with the Z axis, the origin of the world coordinate system is placed on the camera. Therefore, the translation vector $\mathbf{T}$ in Equation (1) becomes a vector of zeroes. The world coordinates of the target C are then measured with respect to the camera. Plugging $[X_C, Y_C, Z_C]^{\mathrm{T}}$ and $\mathbf{T} = [0, 0, 0]^T$ into Equation (1), the scale factor s_C is determined by solving the third row of this system of equations.

To determine ΔX_C and ΔY_C movements in Equation (2), the scale factor for the undeformed position needs to be known for each target. It is not practical to identify the world coordinates of each target when doing multipoint displacement measurements and calibrate the scale factor individually. As an alternative approach, it is useful to note that Equation (2) can also be used to describe the distance between two targets in the object plane. In this case, ΔX_C and ΔY_C

denote the distance between targets C and C' on the object plane whereas $[u_C, v_C, 1]^T$ and $[u_{C'}, v_{C'}, 1]^T$ denote their respective coordinates on the image plane. By using the previously calibrated scale factor s_C, the scale factor $s_{C'}$ for the target C' can then be determined by solving the third row of Equation (2). This can be done for all monitoring targets lying on the same object plane. Therefore, by using two vanishing points in the image and single *XYZ* coordinate for a target on the object, multiple targets on the object plane can be calibrated.

Once the calibration is complete, Equation (2) can be used to solve for the dynamic displacements ΔX_C and ΔY_C for an arbitrary monitoring target C. For each image frame, the deformed coordinates $[u_{C'}, v_{C'}, 1]^T$ are determined with DIC. The scale factor $s_{C'}$ is then determined by solving the third row of Equation (2), with the known scale factor s_C of the undeformed target. Then, the first two rows of Equation (2) are solved to determine in-plane metric displacements ΔX_C and ΔY_C.

3 | SURVEY OF RELEVANT DIC ERRORS FOR MONITORING MASONRY BRIDGES

In ideal conditions, modern DIC algorithms can track in-plane movements of targets in the image plane to less than 0.01 pixel precision.[12] However, various factors can affect DIC measurements, particularly in the field, where environmental conditions (e.g., lighting) are difficult to control. In addition, monitoring masonry bridges with DIC pose notable challenges. Masonry bridges are composed of stiff and discontinuous components, and this necessitates the measurement of small magnitude (submillimetre) relative displacements at many locations on the bridge to track the behaviour of different components.

In order to understand the influence of various factors on displacement measurements, it is necessary to identify the most relevant sources of errors. In Table 1, relevant errors and their qualitative influence on measurement resolution, repeatability, and accuracy are surveyed. Here, resolution refers to the smallest displacements that can be measured by the system. This can be calculated from data as standard deviation of measurement noise. Repeatability refers to the measurement variability in response to near-identical physical movement. It relates strongly to resolution, although it is also influenced by additional factors. On the other hand, accuracy evaluates discrepancy of measurements from ground truth, generally measured by a more reliable technique. It should be noted that the accuracy of both absolute displacement and relative displacement (e.g., strain) measurements is evaluated in Table 1. The influences of various different errors on resolution, repeatability, and accuracy are ranked 1–3 according to their prominence based on literature.[12] The possible sources of error are categorised into three sections: video acquisition, video processing, and structural actions.

Measurement errors can occur due to a nonoptimal set-up of the equipment for video acquisition. In particular, tracking performance is affected by the brightness of targets; resolution and repeatability are severely reduced for overexposed and underexposed targets.[26] For a good tracking performance, it is important to achieve a high contrast in each greyscale target by applying the correct exposure setting. In a similar manner, it is advisable to maintain the targets in focus for a better tracking performance. When monitoring multiple targets located at different distances from the camera, it is beneficial to utilise the smallest aperture possible to obtain a large depth of field. However, previous studies demonstrate that tracking performance is not significantly reduced for out of focus and blurry targets.[27]

Several issues arise when multiple targets on the structure are monitored from close range. Past studies demonstrate that for wide angle lens configurations (which may be necessary for a wide field of view), the radial distortions at the edges of the image may have a strong influence on relative displacement accuracies.[28] Lens distortion coefficients can be corrected through a lab calibration.[29] Alternatively, postprocessing techniques can be used to calibrate simple distortion models, such as the single-parameter division distortion model,[30] using straight lines in the image.[31] Another issue related to equipment set-up for close range monitoring concerns the movement of cameras. During the passage of a train, the ground underneath the structure may vibrate and this may cause movement of the nearby camera. Similarly, wind-induced vibrations of the tripod may also disturb the camera. These small movements, likely imperceptible to the naked eye, can cause appreciable changes in the position of targets in the image plane, and these changes are registered as displacements. When it is not possible to eliminate camera movements by a good set-up, they can be corrected during postprocessing. A simple correction method is to measure relative displacements in the object plane, thereby rendering the influence of translational camera movement parallel to the image plane negligible.[18,32] However, this approach does not account for all potential translational and rotational movements of the camera. To do this, general camera movements can be calculated from several stationary targets that are located in the image by using a

TABLE 1 Qualitative evaluation of digital image correlation (DIC) errors and their influence on resolution, repeatability, and accuracy alongside techniques for mitigation of these errors

Influence DIC errors	Resolution	Repeatability	Accuracy (absolute)	Accuracy (relative)	Error mitigation techniques (during set-up and processing)
Video acquisition					
Equipment set-up (e.g., exposure)	2	2	2	2	• Set-up: Ensure correct camera exposure, aperture and focus settings are used.
Lens distortion (e.g., radial distortion)	1	1	1	2	• Set-up: Use longer focal lengths where possible. • Processing: Determine distortion constants from straight lines. Remove effects during postprocessing.
Camera movement (e.g., translation and rotation)	1	3	3	1	• Set-up: Place camera firmly on a stable location. • Processing: Identify camera movements from stationary targets in the image. Investigate relative movements.
Environmental effects (e.g., light)	1	3	3	3	• Set-up: Allow autoexposure. Monitor in shade for short durations. • Processing: Remove low frequency drifts separately for all targets.
Video processing					
Target quality	3	3	3	3	• Set-up: Utilise artificial targets. • Processing: Determine appropriate target location and size.
Metric calibration	1	1	3	3	• Set-up: Conduct a detailed geometric survey. • Processing: Assess the camera extrinsic parameters and reconstructed features.
Structural actions					
Elastic deformations and rigid body rotations	1	1	1	1	• Processing: Use higher order shape functions for digital image correlation.
Out-of-plane movement	1	1	3	3	• Set-up: Utilise a stereoscopic camera set-up. • Processing: Make independent measurements and correct data.

Note. The colour-coded units 1, 2, and 3 indicate increasing influence of DIC errors on the relevant category.

procedure described by Yoneyama and Ueda.[17] However, finding multiple stationary targets within the vicinity of a structure can be challenging in the field, particularly due to environmental effects, which are discussed next.

Even when the equipment is set up optimally, environmental errors during video acquisition can affect measurement repeatability and accuracy.[12] In field applications, the lighting conditions can change in a matter of seconds and cause erroneous tracking of targets. Allowing automatic determination of exposure (autoexposure) to maintain similar levels of illumination in the image can be an effective mitigation technique.[32] However, autoexposure is less effective when more than one target are monitored. In this case, for each individual target, low frequency drift due to lighting changes may be removed from data with high pass filter or a linear baseline during postprocessing. However, it is not possible to comprehensively correct for such errors, as changes in lighting conditions may not follow a clear trend. Therefore, when monitoring under natural light conditions in the field, it is beneficial to monitor targets in the shade and for brief periods. If the influence of varying ambient light is significant, artificial lighting and optical bandpass filtering solutions, which suppress the varying ambient light with a constant monochromatic light, can be considered.[26] Alternatively, different subpixel tracking techniques that may reduce the influence of ambient light fluctuations on displacement intensity can be used,[22,33–35] although these investigations are beyond the scope of this survey.

Video processing errors can also affect measurement quality. For instance, it is well known that the size and pattern of chosen targets can affect measurement resolution as well as accuracy.[36] Depending on scale and lighting conditions,

natural brick and mortar surfaces may represent good texture for tracking. In this case, the size of a single brick and mortar assembly in the image should not be smaller than 20 pixels. In addition, previous studies[37] suggest that the size of targets should be larger than 40 by 40 pixels for a good tracking performance. During postprocessing, by comparing resolution (measurement noise in pixels when the structure is stationary) to the required pixel precision, the suitability of the determined natural pattern targets for tracking can be evaluated. If natural pattern targets are not suitable, suitably sized artificial targets may be installed on the structure. Axisymmetric bullseye patterns printed on matte paper have been used in the past for this purpose.[37]

Once suitable targets have been determined, it is essential to evaluate the accuracy of the calibration of extrinsic camera parameters. If these parameters are not accurate, displacements in pixel units will be incorrectly scaled to metric units. This may induce large displacement errors, which will primarily influence the absolute and relative displacement measurement accuracy. The magnitude of errors induced depends on the particular set-up (e.g., the degree of error in the estimation of camera rotation angles) and structural actions (e.g., the magnitude and direction of in-plane displacements). To minimise potential errors in calibration, the distances between features in the monitored plane can be evaluated. The metric distances from the camera reconstruction can be compared to geometric survey data (e.g., from a laser scanner) to identify the accuracy of the calibration. In addition, the pitch and roll angles of the camera, which should be measured during equipment set-up, can be compared with the angles calculated from the calibrated rotation matrix.

Structural actions can also influence measurement results. In particular, rigid body rotations may alter the visual characteristics of pixels, preventing successful tracking of targets in the image when low-order shape functions are used for DIC. This may be prevented by using higher order shape functions, which allow the rotation of targets while matching target locations between different images.[21] Past experience suggests that the influence of rotations on tracking performance is negligible due to the small magnitude of movements. The other source of structural error is out-of-plane movement. If there are out-of-plane movements in the object plane, DIC registers them as in-plane movements, resulting in inaccurate measurements. Previous studies on DIC errors[38] have noted that out-of-plane movement can have significant influence on measurement, particularly at the edges of the image. In these cases, it is necessary to utilise alternative measurements to determine the magnitude of out-of-plane movements. Thereafter, their influence on the in-plane measurements can be corrected. However, if it is known ahead of monitoring that out-of-plane movements are likely to be significant, it may be more suitable to use the 3D DIC technique with a stereoscopic camera set-up[38] which allows the determination of three components of displacements of targets that are shared between two cameras. However, 3D DIC systems with stereoscopic camera set-up come with some disadvantages. They are harder to set up in the field, they limit the area in the camera field of view where displacement monitoring can be carried out, and they typically provide lower measurement resolutions than 2D DIC.

Table 1 does not present an exhaustive list of DIC errors. For instance, errors due to correlation algorithms are omitted, as these errors are typically small.[12] However, the most relevant sources of errors for field monitoring of masonry bridges were identified in Table 1, alongside potential error mitigation techniques. An application of 2D DIC to a masonry bridge is discussed next to illustrate these aspects.

4 | FIELD SET-UP AND DATA PREPROCESSING

Marsh Lane Viaduct is a brick masonry viaduct on the Leeds–Selby route in Yorkshire, UK. It was constructed in various phases during the 19th century. The two arch spans investigated were constructed as part of the North Eastern Railway Leeds Extension and are approximately two miles away from Leeds Central Station. The bridge has a route availability rating of 10, which qualifies it for carrying trains with 25 ton axles. Therefore, all passenger trains on the network can use this line. The bridge carries two tracks and has a speed limit of 55 km/hr.

Some key characteristics of Span 38, which will be investigated in detail, are shown in Figure 2a. The arch has a span of 7.7 m, a rise of 2.1 m, and a width of 8 m. The arch barrel is 0.5 m thick and constructed of four rings. Above the arch barrel, there is backing and soil fill, supporting the ballasted track. A particular characteristic of the Marsh Lane Viaduct is the presence of central relieving arches in its piers. Signs of vertical sagging movements can be observed above these relieving arches, such as a longitudinal crack that emanates from the relieving arch (the location of which is sketched on Figure 2a). The longitudinal crack is about 3 cm wide at the springing and becomes a hairline crack at the quarter span. Longitudinal cracking indicates spreading of the relieving arch and rotation of the piers towards the spandrel walls during dynamic loading. Recently, the relieving arches were filled in with concrete, and the longitudinal

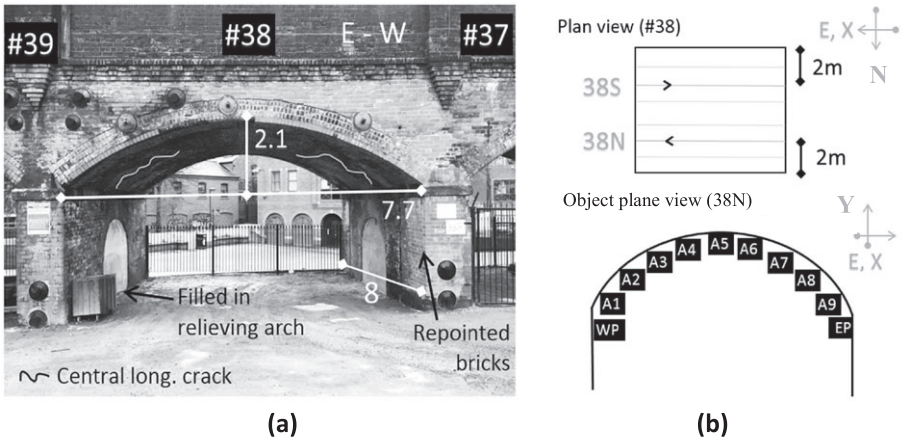

FIGURE 2 (a) A photo showing Arch 38. Annotations draw attention to critical dimensions and recent maintenance works. (b) The schematics show the object planes and the associated targets

cracks were grouted, presumably to arrest these movements. There are also other signs of visible damage in the viaduct, such as transverse cracks at the quarter span points, large areas of repointed bricks at piers, and steel ties and horizontal cracks at the spandrel walls.

As demonstrated in Figure 2a, the damage observed in the Marsh Lane Viaduct was distributed, and various structural interventions (e.g., filling in relieving arches) were made to limit further damage. Therefore, it was necessary to monitor many different locations of the structure to understand the dynamic response of the viaduct in its current degraded conditions. This presented an ideal case for the use of the DIC technique. The commercial DMS system by Imetrum was used for this purpose. The system hardware consisted of two industrial-grade Allied Vision GigE video cameras and a system controller. The camera sensors featured 2,048 × 1,088 pixels with an 11.26 × 5.98-mm-sized sensor and allowed data acquisition at a frame rate of 50 Hz. Imetrum Video Gauge software was used to control the hardware and perform DIC on the image plane. Further data processing was conducted by the authors using custom-written scripts in MATLAB.

Figure 2b demonstrates the object planes that were monitored using DIC. These vertical planes are located under the centreline of tracks and align with the bridge longitudinal axis. Due to significant stiffness of arch bridges in their transverse direction, it was expected that transverse movements (i.e., out-of-plane ΔZ movements with respect to the object plane) would be negligible; therefore, 2D DIC was used. At each monitoring section, the monitoring targets WP and EP measure the horizontal (ΔX) and vertical (ΔY) pier top movements. Similarly, consecutively placed targets A1–A9 (proceeding west to east) measure the displacements in the same object plane. With such a configuration of monitoring targets, the behaviour of the whole arch could be measured. This is demonstrated in Figure 3a, where the field of view of one of the cameras is shown. In addition to DIC, a fibre optic cable that measures strain between consecutive monitoring targets (e.g., A1–A2 and WP–EP) is also visible in this figure. The cable measures strain between metallic clamps located at nearby monitoring locations (i.e., A1–A9, EP, and WP), with 1-$\mu\varepsilon$ resolution and 250-Hz sampling rate, using the Fibre Bragg Grating (FBG) technique.[39] This higher precision fibre optic cable gave an indication of the load distribution in the structure and was also used to evaluate the accuracy of the DIC system.

Figure 3b shows how the camera was positioned to capture the targets in each monitoring plane. An 8-mm-wide lens was used for achieving the required field of view. The camera and the lens were placed on a tripod on the ground at midspan, approximately under the spandrel wall and 6 m away from the object plane. The camera was then tilted up at an angle to capture the desired monitoring targets with a perspective view. The arrangements of the cameras for two different monitoring configurations are shown in Figure 3c. In Configuration 1, two cameras record the arch displacements in the longitudinal planes 37N and 38N in synchrony. Both cameras were tilted approximately 16° in pitch direction and less than 1° in roll direction, as measured by the tilt integrated laser rangefinder. In Configuration 2, the two cameras record the displacement response of 38N and 38S. In this case, the 38N and 38S cameras were tilted approximately 16° and 8° in the pitch direction, respectively, and less than 1° in the roll direction.

The object plane shown in Figure 3a features natural brick and mortar patterns suitable for tracking as well as artificial axisymmetric bullseye targets installed on the structure. These targets were 20 by 20 cm, so that their reflection on the image plane corresponds to an area of 40 by 40 pixels. This is shown in Figure 4a, where artificial and natural targets A5 are located side by side around the crown area of the arch of object plane 38N. In Figure 4b, the measurement

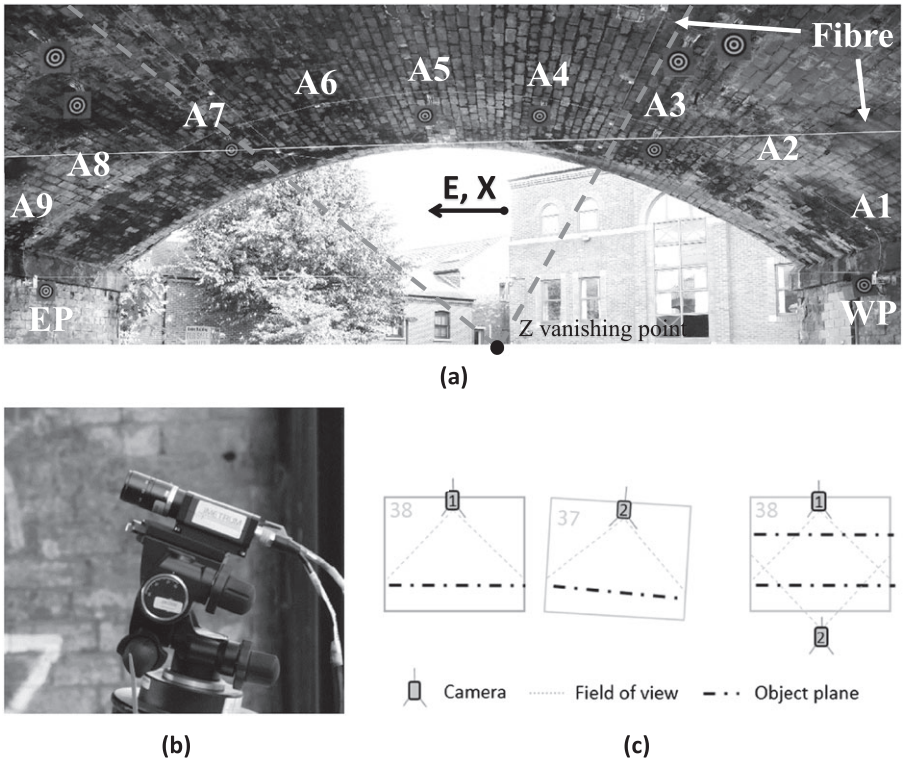

FIGURE 3 (a) A photo showing the object plane 38S. The annotations denote the unique ID for each clamp, where fibre optic cables are fixed and digital image correlation (DIC) targets are located. (b) Another photo shows the side view of the camera, whereas (c) the schematic plan views outline the location of the camera for each DIC configuration

resolutions of these natural and artificial patterned targets are determined by comparing the Δu displacement measurement (movement of the target along the U coordinate of the image plane in pixel units) noise at a time when there were no trains on the viaduct. The time history data, spanning 5 s, indicate negligible differences between targets. The resolution values of measurements from artificial and natural patterns (0.018 and 0.016 pixels) are larger than 0.01 pixels. A resolution of less than 0.01 pixels was achieved in Figure 4d when 80×80 pixel targets are used. However, the 40×40 pixel natural target resolution was deemed acceptable for the current application. Therefore, for consistency, all monitoring targets on the arch (A1–A9) were defined as 40×40 pixel targets located on the natural brick pattern. They lie adjacent to the artificial bullseye targets and metallic fibre optic clamps, as illustrated in Figure 4a. Based on a 0.02 pixel resolution, the expected metric resolution for relative displacement measurements was estimated as 0.12 mm in this configuration.

As shown in Figure 3a, monitoring targets were located in the shade. This ensured similar levels of illumination on different targets. Therefore, a suitable camera exposure could be determined to track all monitoring targets. However, to maintain this exposure, larger apertures were necessary and some targets were not in complete focus. Furthermore, in order to minimise the influence of changing lighting conditions on the displacement measurements by the DIC system, autoexposure was allowed. However, changing light effects influenced targets on the piers more than the targets on the arch. This is demonstrated with a 1-min recording of the Δu displacement of monitoring target EP. Both the natural and artificial targets are not in focus (see Figure 4e), although their resolution is similar to the above cited values. In addition, the artificial EP target was faced away from the light source and was not affected by the changes in illumination. However, as demonstrated by the time history trace in Figure 4f, the natural EP target demonstrated significant low frequency drift of 0.1 pixels within 1 min. During this time, a train passed over the viaduct causing lateral movements less than 0.05 pixels. Therefore, despite the careful set-up of the equipment, the environmental changes were more significant than the displacements in the structure for the natural pier targets. Fortunately, lighting errors only affected pier data and, due to their short length, could be corrected with a linear baseline. Therefore, this was adopted as a standard procedure for processing of all monitoring targets. However, in order to further minimise errors, the artificial targets were used for WP and EP positions. Finally, Figure 4g shows a stationary target, located close to the monitoring plane. Its Δu response during a train passage (see Figure 4h) indicates a similar resolution of 0.02 pixels, suggesting that

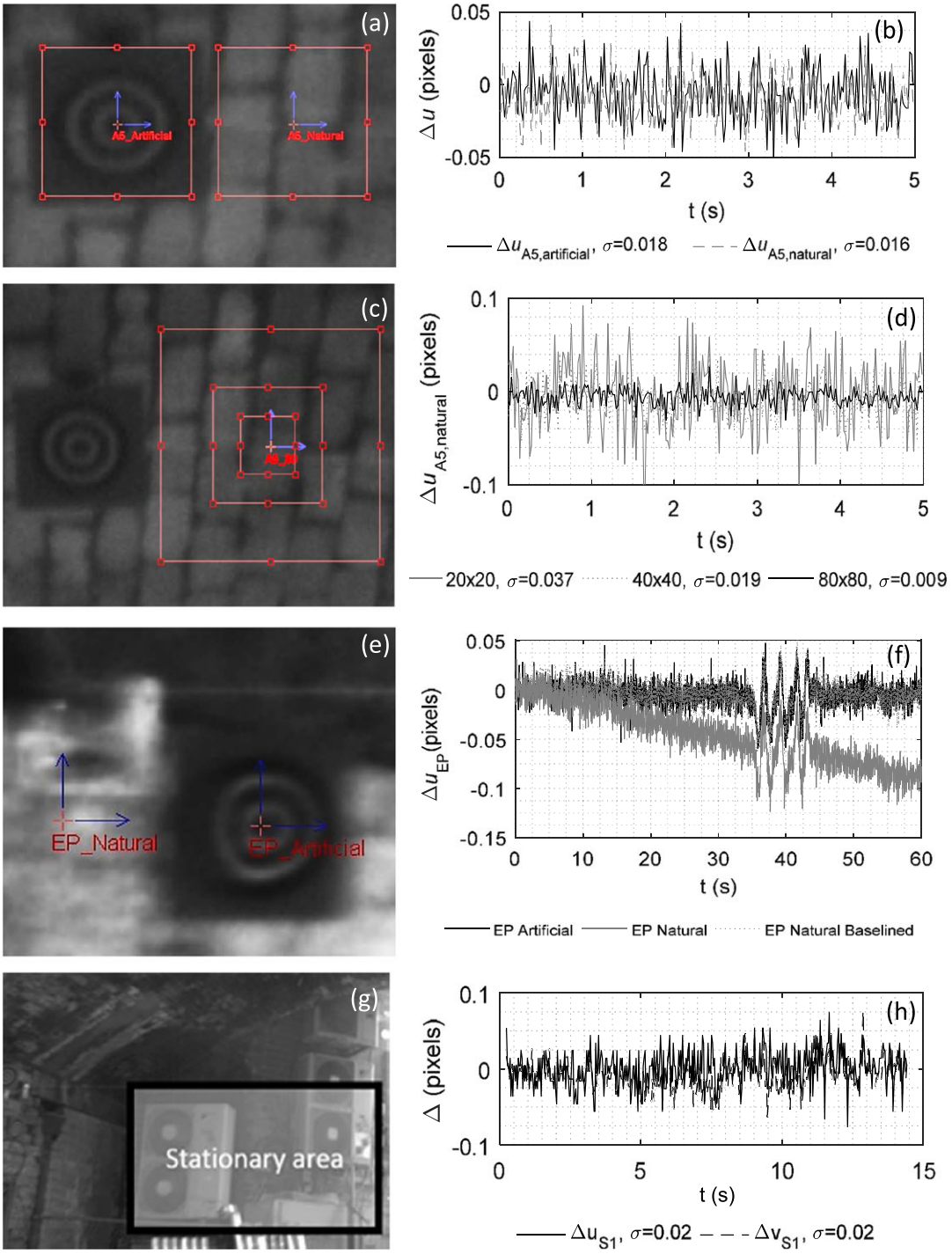

FIGURE 4 (a) A video snapshot showing artificial and natural monitoring target A5 and (b) a 5-s time window where measurement noise is observed for these targets. (c) Another video snapshot and (d) a time history plot show the measurement noise from three natural monitoring targets with different sizes. (e) Artificial and natural monitoring targets and (f) a 60-s time window where drifts induced by lighting changes are removed with a linear baseline are also shown. Finally, (g) a stationary area in the image and (h) tracking of target S1 in this area are shown

camera movements were negligible. Furthermore, because only relative displacements will be examined in this paper, potential camera movement influence is expected to have negligible impact on measurements and will not be discussed further.

After setting up the cameras and monitoring targets, calibration was necessary. It was conducted using the technique presented earlier in Section 2, which is illustrated in the following. For retrieving the rotation matrix, two lines parallel to the Z axis and passing through the masonry bedding joints around A3 and A7 were manually determined

(see the two grey dashed lines in Figure 3a). Their intersection is the *Z* vanishing point, which is shown at the bottom of the image frame in Figure 3a. After determining the pixel coordinates of the vanishing points for both *Z* and *Y* axes, the full rotation matrix was constructed using Equation (4) and the pitch, yaw, and roll angles were determined. This was done for the object planes in each camera configuration employed during 2 days of monitoring. In addition, because the object planes where artificial and natural targets are located are offset from one another, different calibrations were made for monitoring targets WP–EP and A1–A9. The results of these calculations are listed in Table 2. A good agreement is observed between the approximate field measurements and the calibration estimations for the pitch and roll angles; the results were within 1.5° of each other. After establishing this agreement, the scale factors were determined for each target in each object plane using the world coordinates of monitoring targets A1 and WP.

Upon completion of the calibration, it was necessary to check the accuracy of the reconstruction. To do this, estimations of geometric characteristics of the bridge from the camera and a geometric survey from a laser scanner can be compared. Span (denoted by δX(WP – EP)) and rise (denoted by δY(A1 – A5) measured as the *Y* distance between A1 and A5) estimations were chosen for this purpose, and these parameters were calculated using Equation (2). Table 2 lists estimates of these distances from calibrations and the percentage error with respect to the laser scan surveys. From the table, it is clear that the half span and rise are estimated with an error less than 5%. This reduces to less than 2% error for the geometry data from object plane 38N, which will be investigated in detail. Considering the centimetre-level accuracy while identifying features in a laser scan survey, these results validate the accuracy of the calibration.

5 | DIC FIELD DATA RESOLUTION, REPEATABILITY, AND ACCURACY

Using the set-up described in Section 4, data were gathered using both DIC and the FBG techniques. A significant portion of the gathered data describe the response of the arches to the Class 185 TransPennine route trains, which run frequently on the Leeds–Selby line. The influence of live passenger load on these trains is small compared with the dead load, and dynamic amplification was not observed due to the relatively stringent speed limitation (55 km/hr). Therefore, to investigate the repeatability and accuracy of measurements, the recorded response of monitoring plane 38N to the Class 185 train will be examined in this section. For this purpose, five datasets for eastbound and westbound trains were chosen, and these are summarised in Table 3.

Figure 5 provides an example of DIC data, by showing the dynamic displacement response of 38N to a Class 185 train from Dataset 1. Figure 5e shows the raw relative displacement between pier tops, denoted by $\Delta(\text{WP} - \text{EP})_{\text{DIC}}$ and calculated along the initial position vector $\overrightarrow{\text{WP–EP}}$ (see Figure 5a for the direction of this movement). Because this vector is near horizontal, the signal describes the span opening and closing as the train moves over the bridge. Similarly, the raw $\Delta Y(\text{A1} - \text{A5})_{\text{DIC}}$ signal is plotted in Figure 5f. $\Delta Y(\text{A1} - \text{A5})_{\text{DIC}}$ denotes the vertical displacement of the crown target A5 with respect to the springing point A1 as the train moves over the bridge. It is calculated along the *Y* component of the initial position vector $\overrightarrow{\text{A1–A5}}$ (see Figure 5a). In the same figure, the relative displacement between two monitoring targets at the crown $\Delta(\text{A4} - \text{A5})_{\text{DIC}}$ is also plotted (see Figure 5a). Consistent with the previous notation, this measurement is along the initial vector $\overrightarrow{\text{A4–A5}}$. Different from the previous signals, this signal is low pass filtered (5-Hz cut-off) to reveal its characteristic trace.

Before evaluating the accuracy of the DIC data, it is useful to briefly interpret these signals. To do this, the schematics in Figure 5b–d demonstrate span opening and vertical crown displacement response at highlighted instances

TABLE 2 A comparison of key dimensions of geometries reconstructed from the camera with the recorded geometry from laser scanning

Object plane	Day	Camera configuration	$\delta\theta_X$ pitch (°)	$\delta\theta_Y$ yaw (°)	$\delta\theta_Z$ roll (°)	δX(WP–EP) span (mm)	Span error (%)	δY(A1–A5) rise (mm)	Rise error (%)
38N	1	1	−15.3	−0.74	−0.83	7,295	0.07	1,207	1.9
38N	1	2	−17.2	1.68	−0.04	7,301	0.02	1,212	1.5
38N	2	2	−14.3	0.98	0.43	7,335	0.48	1,246	1.3
37N	1	1	−16.2	−1.0	−1.5	7,658	4.9	1,323	3.4
38S	1	2	−6.7	1.4	−0.6	7,377	1.4	1,330	3.9
38S	2	2	−7.5	1.6	−0.3	7,046	3.1	1,240	3.4

TABLE 3 Properties of the investigated datasets

Datasets	Train direction	Configuration	Speed (km/hr)	Day
1	E	1	49.7	1
2	E	1	50.2	1
3	E	2	46.5	1
4	E	2	39.6	1
5	E	2	37.7	2
6	W	1	22.5	1
7	W	1	22.4	1
8	W	2	34.1	1
9	W	2	48.3	1
10	W	2	23.0	2

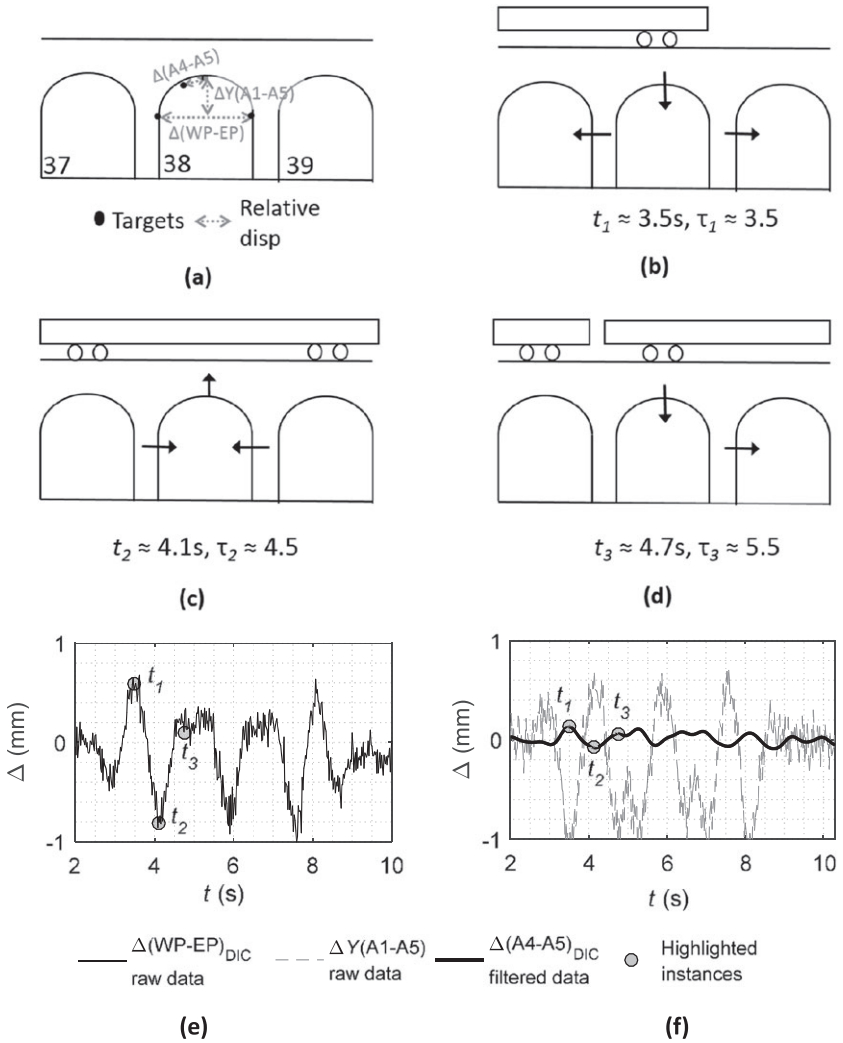

FIGURE 5 (a–d) Schematics that illustrate the location of DIC measurements and the location of the axles of a Class 185 train at critical instances. (e–f) Time history plots from Dataset 1 highlight the span opening and relative crown and springing displacements in these instances for Arch 38

t_1, t_2, and t_3. These drawings illustrate the location of axles of the first train carriage as it passes over Arch 38N. At the instant $t_1 = 3.5$ s, the leading axle is above the crown of Arch 38N whereas the back axle of the same carriage is two spans away. Therefore, the 38N span opens, whereas the crown goes down. According to the A4–A5 relative displacements, this causes opening (tension) at the crown. At the next instant $t_2 = 4.1$ s, the front and back axles of the front car are above the crown of the neighbouring Spans 37 and 39. This causes the piers to push in, the 38N span to close, and

crown to go up with compressive strains. Afterwards, at $t_3 = 4.7$ s, the back axle of the first car is above the crown of 38N and the front axle of the car is above the crown of the neighbouring 37N. Therefore, the pier between Arches 37 and 38 cannot move laterally, but the eastern pier of 38N moves outwards, causing the span to open. Here, the span opening and the accompanying crown vertical movement and strain are smaller than at $t_1 = 3.5$ s, as only one of the piers is moving. After this, similar patterns of response are repeated as the other train carriages pass over the arch. Further discussions regarding the structural behaviour of the viaduct can be found elsewhere.[40,41]

Figure 5 demonstrates the key influence of span opening and closing on the arch response using DIC data. In Figure 6a, the unfiltered span opening/closing time histories recorded by the DIC and FBG techniques for Dataset 1 are plotted. Relative displacements are calculated from multiplying the strain data from a single FBG node with the reconstructed distance δ(WP – EP) from the camera. A good agreement is observed between the two relative displacement signals, where both techniques demonstrate the same pattern of response. However, the DIC data underestimate the span opening magnitude. It is also noteworthy that the DIC data are noisier and indicate residual span closing after the passage of the train. The periodogram of the DIC and FBG signals, presented in Figure 6b, verifies this. The noise floor of the DIC data is higher than that of the FBG data, particularly for frequencies greater than 5 Hz and smaller than 0.25 Hz. A finite element model of the structure (not shown) indicates that the first vibration mode frequency of the viaduct would be expected to be in the frequency range 15–30 Hz. A small peak can be observed at 27 Hz for the FBG data although it has negligible influence. This confirms that the response of Arch 38N to the Class 185 train travelling at $v = 49.7$ km/hr is quasistatic with negligible dynamic amplification. Therefore, the data can be filtered to focus on the low frequency response without causing loss of information.

To compare the span opening and closing response from similar datasets listed in Table 1, it is useful to normalise the time t with the time it takes for the axles of a train to travel from the centreline of one arch pier to the next. This can be determined from the train speed v and the distance between pier centrelines $d_{cr} = 8.55$ m. The normalised time τ is expressed as $\tau = \frac{v}{d_{cr}}t + \tau_o$. Here, τ_0 denotes the translation of the dataset, so that the first span opening peak, detected at t_1 with a peak fitting algorithm in Figure 5e, would appear at the normalised time $\tau = 3.5$. The next peak occurs at time t_2 in Figure 5e where the span is closing, and this corresponds to $\tau = 4.5$, where the axles travelled one span further from $\tau = 3.5$. Because it is only necessary to capture this cyclic quasistatic movement, all data were filtered with a cut-off frequency $f_c = \frac{2v}{d_{cr}}$. The Dataset 1 time history for the FBG and DIC data after normalisation is plotted in Figure 6c. The normalised periodogram is plotted in Figure 6d, where the frequency is normalised with $\frac{v}{d_{cr}}$. After filtering, a smoothening of the data above the normalised frequency of 2, and a clear reduction in the noise floor, is observed.

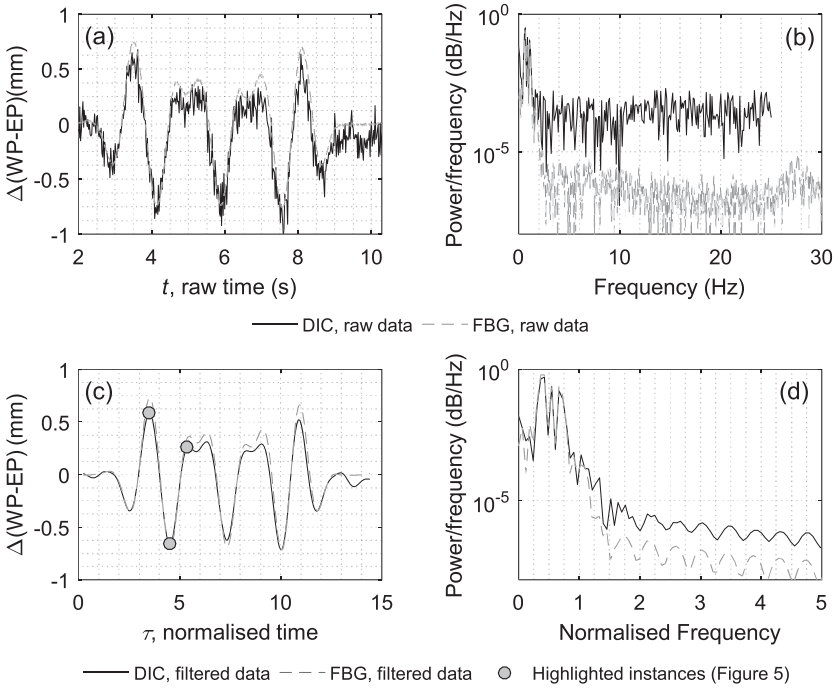

FIGURE 6 Span opening/closing time histories and periodograms from Dataset 1: (a–b) raw data and (c–d) filtered and baseline-corrected data from digital image correlation (DIC) and fibre Bragg grating (FBG) sensing techniques

The normalised and filtered time histories of the 38N span opening from Datasets 1–5 (see Table 1) are directly compared in Figure 7a–b. Although all of these datasets describe response to an eastbound Class 185 train with similar speeds in the range between 30 and 55 km/hr, they were gathered using different camera configurations on separate days. The distinct FBG datasets indicate strikingly similar response. DIC datasets show more significant discrepancies. First of all, notable measurement noise exists in the DIC measurements, even when the span is outside the zone of train axle influence, when $\tau < 2$ or $\tau > 12.5$. The standard deviation of the raw data noise approximately defines the resolution of the system and has an influence on the subsequent response estimation. Furthermore, the span opening and closing indicated for the instances $\tau_1 = 3.5$ and $\tau_2 = 4.5$ (see Figure 4) vary appreciably for the DIC data, whereas they are similar for the FBG data. The standard deviation of the peak magnitudes for the filtered datasets can be used to quantify the repeatability of the data. Finally, differences between the span opening and closing magnitudes recorded by the DIC and FBG systems at $\tau_1 = 3.5$ and $\tau_2 = 4.5$ may be used to quantify the accuracy of the DIC system. This can be achieved by computing the difference between two filtered signals $\Delta(\text{WP} - \text{EP})_{\text{DIC}} - \Delta(\text{WP} - \text{EP})_{\text{FBG}}$ for each dataset at the specified instances and computing the mean difference for all datasets. This difference is plotted in Figure 7c for Dataset 1, where the left axis shows the span opening and closing recorded by the FBG system and the right axis plots the difference between DIC and FBG measurements for the same signal. Figure 7c demonstrates the general underestimation of span opening by DIC technique by close to 0.15 mm. Similarly, other common measurements of the DIC and FBG systems may be compared to quantify the accuracy. One of them is the relative displacement measurement between two crown targets, $\Delta(\text{A4} - \text{A5})$. The $\Delta(\text{A4} - \text{A5})_{\text{FBG}}$ signal can be calculated by multiplying the strain with the reconstructed A4–A5 axial distance from the camera. This signal and the difference between FBG–DIC signals $\Delta(\text{A4} - \text{A5})_{\text{DIC}} - \Delta(\text{A4} - \text{A5})_{\text{FBG}}$ for Dataset 1 are plotted in Figure 7d. Here, discrepancies in the measurements are less than 0.1 mm.

The resolution and repeatability of the DIC and FBG systems were calculated using raw $\Delta(\text{WP} - \text{EP})$ and $\Delta(\text{A4} - \text{A5})$ signals and are summarised for Datasets 1–5 and 6–10 in Table 4. The typical resolution of the DIC system for relative displacement measurements is around 0.10 mm, similar to the previous prediction of 0.12 mm in Section 4. The data confirm that the resolution of the FBG system is around 1 $\mu\varepsilon$, and its relative displacement resolution is proportional to the strain measurement gauge length. For $\Delta(\text{A4} - \text{A5})$, the gauge length is about 1.3 m and the resolution corresponds to 0.001 mm. For $\Delta(\text{WP} - \text{EP})$, the gauge length and resolution are 7.4 m and 0.006 mm, respectively. Furthermore, the repeatability of data is evaluated by comparing the standard deviation of the peak at $\tau_1 = 3.5$. The repeatability of this peak varies for the span and crown relative displacement measurements; for FBG measurements, repeatability is larger than the resolution, indicating that differences due to train live loads are likely influencing response. Nonetheless, according to data, both span and crown relative displacements are repeatable to 0.03 mm. In contrast, for DIC

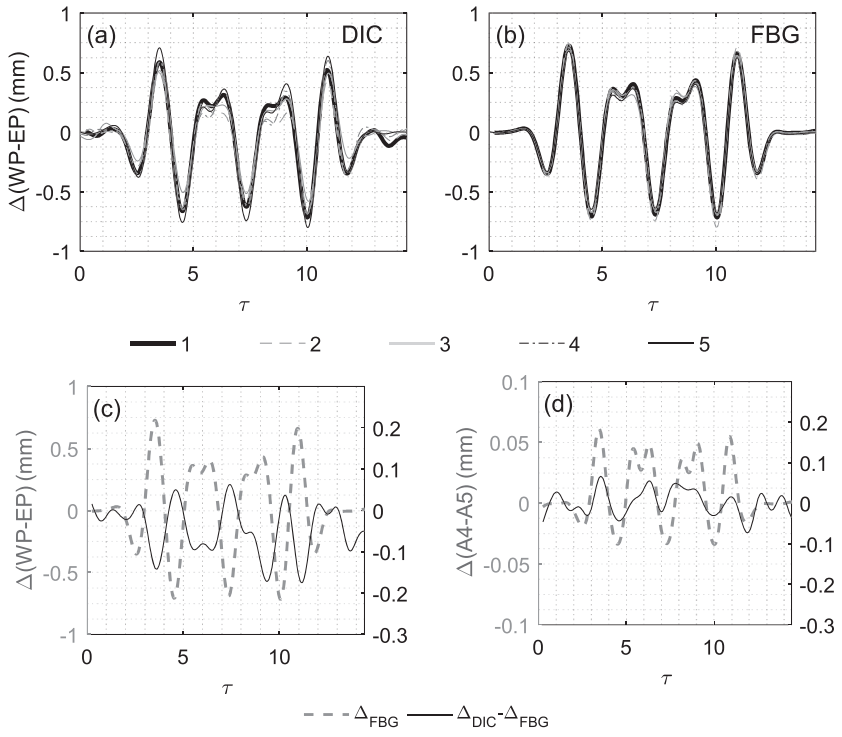

FIGURE 7 Span 38 opening/closing normalised time histories from Datasets 1–5: (a) using digital image correlation (DIC) and (b) fibre Bragg grating (FBG) sensing techniques. (c–d) The differences between DIC and FBG measurements are shown for the span opening/closing and relative crown displacements from Dataset 1

TABLE 4 The resolution, repeatability, and accuracy of the DIC system (with respect to the FBG system) for Datasets 1–10

	Resolution[a] (mm)	Magnitude[b] (mm) $\tau = 3.5$	Repeatability[c] (mm) $\tau = 3.5$	Accuracy[d] (mm) $\tau = 3.5$	Accuracy[d] (mm) $\tau = 4.5$
Datasets 1–5					
$\Delta(\text{WP–EP})_{\text{DIC}}$	0.091	0.580	0.082	−0.129	0.045
$\Delta(\text{WP–EP})_{\text{FBG}}$	0.006	0.709	0.026		
$\Delta(\text{A4–A5})_{\text{DIC}}$	0.107	0.122	0.037	0.062	−0.031
$\Delta(\text{A4–A5})_{\text{FBG}}$	0.001	0.060	0.002		
Datasets 6–10					
$\Delta(\text{WP–EP})_{\text{DIC}}$	0.089	0.302	0.041	0.0726	0.0768
$\Delta(\text{WP–EP})_{\text{FBG}}$	0.005	0.229	0.024		
$\Delta(\text{A4–A5})_{\text{DIC}}$	0.106	0.066	0.019	0.0481	−0.004
$\Delta(\text{A4–A5})_{\text{FBG}}$	0.001	0.018	0.002		

Note. FBG = fibre Bragg grating; DIC = digital image correlation.

[a]Resolution is the average standard deviation of measurement noise from five datasets.

[b]Magnitude is average peak signal magnitude around $\tau = 3.5$ from five datasets.

[c]Repeatability is the standard deviation of the peak magnitude located around $\tau = 3.5$ from five datasets.

[d]Accuracy is average DIC peak measurement error with respect to FBG system from five datasets.

measurements, repeatability is similar to or smaller than the resolution. For instance, for Δ(WP – EP) signal, the repeatability of the DIC and FBG systems are calculated respectively as 0.08 and 0.03 mm. This demonstrates the approximate correlation of resolution and repeatability, suggesting that variability between DIC peaks are largely due to system resolution.

As mentioned earlier, systematic differences were noted between the magnitudes of relative displacement peaks measured by the DIC and FBG systems. For the given camera configuration, the FBG resolution and repeatability are higher; the accuracy of DIC system is determined with reference to the FBG system. This is done by evaluating the mean difference between data peaks at $\tau_1 = 3.5$ and $\tau_2 = 4.5$ for relative displacements at span and crown from the corresponding datasets. The calculated accuracy results are listed in Table 4. From the table, the DIC data underestimate the span opening, while it captures the span closing reasonably well. Furthermore, the relative displacements at the crown are generally overestimated, although by smaller amounts. The differences between measurement systems are particularly pronounced for Datasets 1–5 at $\tau_1 = 3.5$, where the train travels east above 38N. The DIC data underestimate the span opening peak by 0.13 mm and overestimates crown relative displacement peak by 0.06 mm on average. It is noteworthy that the span opening displacement errors are larger than measurement resolution and correspond to approximately 20% error with respect to the FBG measurements. Similarly, the crown relative displacements from DIC demonstrate close to 100% error. These errors were shown earlier in Figure 7c–d, which demonstrated that they are systematic and do not correspond to random measurement noise.

In Table 4, similar analyses are also conducted for object plane 38N using Datasets 6–10, where the train travels west on the southern tracks over 38S. For these datasets, measurement magnitudes are smaller and errors are typically within system resolution. However, significant errors are also observed. Therefore, in the next section, postprocessing methods to correct these errors will discussed.

6 | DATA POSTPROCESSING TECHNIQUES TO CORRECT DIC ERRORS

The examination of DIC data resolution, repeatability, and accuracy in Section 5 demonstrated that the accuracy of relative displacement measurements is influenced by errors. Since errors due to equipment set-up, lighting effects, target quality, camera movements, and metric calibration were already minimised in Section 4; other sources of error were considered. As listed in Table 1, two remaining sources of errors that may influence relative measurement accuracy are lens radial distortions and out-of-plane movements. These errors are discussed next, with an aim to quantify and compensate for their influence on measurements.

6.1 | Radial distortion

Projective geometric transformation of the object plane by a pinhole camera model (Equation (1)) preserves the collinearity of points in the image plane. In this model, straight lines in the object plane remain straight in the image plane. However, in reality, straight lines are distorted in the image plane, due to imperfections in lens curvature. In particular, distortions can be significant for short focal length lenses, where objects are distorted symmetrically in the radial direction with respect to the principal point (e.g., centre of the image). A negative radial distortion causes barrel distortion, where image magnification decreases with increasing distance from the principal point. In this case, straight lines bulge outwards from the centre of the image. In contrast, positive radial distortion causes pincushion distortion, where straight lines bulge inwards towards the centre of the image.

The use of an 8-mm focal length lens in Marsh Lane Viaduct resulted in noticeable radial distortion. The distortion was evident in the fibre optic lines, which measured relative displacement between two piers, Δ(WP – EP) (see Figure 8a, near top edge of image). These fibre optic lines are pre-tensioned and are therefore straight, although they displayed the distortion pattern shown in Figure 8b in the image plane. This distortion pattern is a combination of barrel distortion, which is dominant in the centre area of the image, and a pincushion distortion, which is dominant around the edges. Because no prior investigation was done in the laboratory, the distorted lines were used to determine distortion coefficients. The single-parameter division model was used for this purpose.[30] This model utilises the undistorted image coordinates p and q, which is a simple transformation of the origin of the UV coordinate system to the principal point at the centre of the image. The undistorted coordinates p' and q' are expressed as a function of the position of distorted image coordinate and a distortion coefficient λ as follows:

$$p' = \frac{p}{1+\lambda(p^2+q^2)}, q' = \frac{q}{1+\lambda(p^2+q^2)}. \tag{5}$$

The simple division model can correct for only one type of distortion when it is applied. Therefore, the model is applied twice, first to correct for the pincushion distortions and then to correct barrel distortions. The unknown distortion coefficients were determined by following an iterative procedure. First, an arbitrary pincushion distortion coefficient was specified in the range 1e-6 to 1e-9. After removing its influence using the division distortion model, the

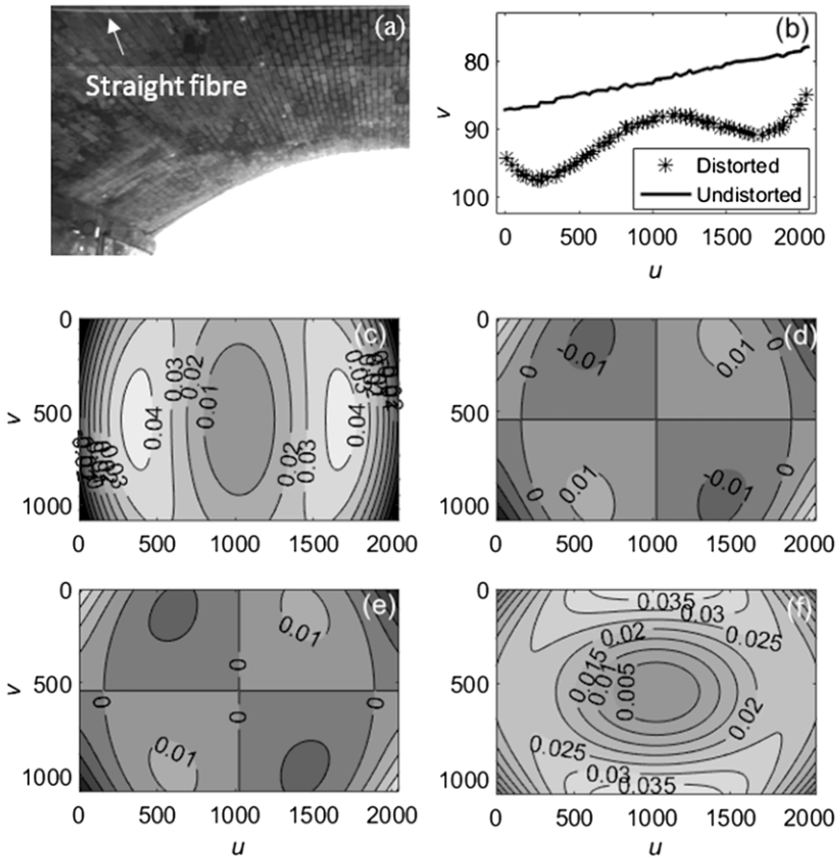

FIGURE 8 Influence of radial distortion on image reconstruction and deformation estimations: (a) a video frame where a straight fibre line is distorted. (b) A plot of the distorted line and its corrected version is then demonstrated. Absolute movement errors due to 1-pixel movement in the (c–d) u and (e–f) v directions are also shown

barrel distortion coefficient was determined. This was achieved by fitting a circle to the pincushion distortion corrected line, as straight lines are expected become arcs due to the influence of barrel distortion.[31] The influence of barrel distortion is then removed, and the linearity of the resultant shape is evaluated with the Pearson correlation coefficient. The pair of distortion parameters that yield a coefficient close to unity for the undistorted fibre optic line describes the radial distortion. The results of this correction with the determined distortion parameters can be seen in Figure 8 b. The determined parameters were validated, as they successfully corrected the distortions present for camera configurations other than the one shown in Figure 8b.

The results discussed in Sections 4 and 5 of this paper were not corrected for the influence of radial distortions. Therefore, it is important to quantify the influence of radial distortions on movement estimations on the pixel plane. This is achieved in Figure 8c,d. These plots show the errors (in pixels) of absolute movement estimations when the distortions are not corrected, when a 1-pixel movement is applied in the image plane along the U coordinate ($\Delta u = 1$). In particular, Figure 8c shows the errors incurred in the estimation of Δu whereas Figure 8d shows the errors in the estimation of Δv. Interesting error patterns emerge as the influences of barrel distortions are largely cancelled out by pincushion distortions. The contour plots show a maximum of 4% error in the estimation of Δu in this case. The errors indicated Figure 8d are smaller and indicate less than 1% error. Similarly, in Figure 8e,d, errors due to a movement of $\Delta v = 1$ are examined. The maximum errors for vertical pixel displacement are around 4% in Figure 8f.

Figure 8 suggests that the radial distortions have some influence on the relative displacement measurement accuracies. However, when radial distortions were corrected, the accuracy of the DIC system, which was discussed earlier in Table 4, did not change significantly (not shown). Therefore, the potential influence of out-of-plane movements is investigated next.

6.2 | Out of plane movements

Out-of-plane movements are known to have a large influence on DIC measurement accuracy, and they may explain the systematic errors in the relative displacement measurements discussed in Section 5. To investigate the influence of out-of-plane measurements on absolute measurement accuracy, simple trigonometric models may be used. Figure 9a presents a side view of the image and object planes, for a camera set-up with a significant pitch angle, and negligible yaw and tilt angles. This set-up is similar to the one used in Marsh Lane Viaduct. Here, a dashed line shows the optical axis of the camera, connecting the principal point to the pinhole.

According to this model, if the target C moves towards the pinhole camera by an amount of $-\Delta Z_C$ (movements towards the camera are defined with a negative sign convention), its position on the image plane changes from v_C to $v_{C'}$. When this pixel movement is scaled to metric movements with an inverse projective geometric transformation, the DIC system erroneously estimates movement of the target from Y_C to $Y_{C'}$. The out-of-plane movement induced apparent displacement is then given by $\Delta Y_{Cop} = Y_{C'} - Y_C$. From simple trigonometry, the relationship between the experienced out-of-plane movements and the apparent in-plane vertical movements due to out-of-plane motion can be approximated as follows:

$$\Delta Y_{Cop} = \Delta Z_C \tan\left(\beta_{Cop}\right) \approx \Delta Z_C \tan(\delta\theta_X + \gamma_{Cv}), \tag{6}$$

where the angle γ_{Cv} is shown in Figure 9 with a negative sign convention. It is calculated as $\gamma_{Cv} = \tan^{-1}\left(\frac{v_c - o_v}{\alpha f}\right)$. For the given camera arrangement, the apparent in-plane horizontal movements due to an out-of-plane movement of ΔZ_C can also be similarly approximated. It is given as

$$\Delta X_{Cop} = -\Delta Z_C \tan(\gamma_{Cu}), \tag{7}$$

where the angle $\gamma_{Cu} = \tan^{-1}\left(\frac{u_C - o_u}{\alpha f \cos\delta\theta_X - \left(v_c - \frac{o_v}{2}\right)\sin\delta\theta_X}\right)$.

Equations (6) and (7) describe the influence of out-of-plane movements on measurement accuracy at the edges of the image. Generally, as the angles γ_{Cu} and γ_{Cv} increase, larger apparent displacements are observed due to out-of-plane

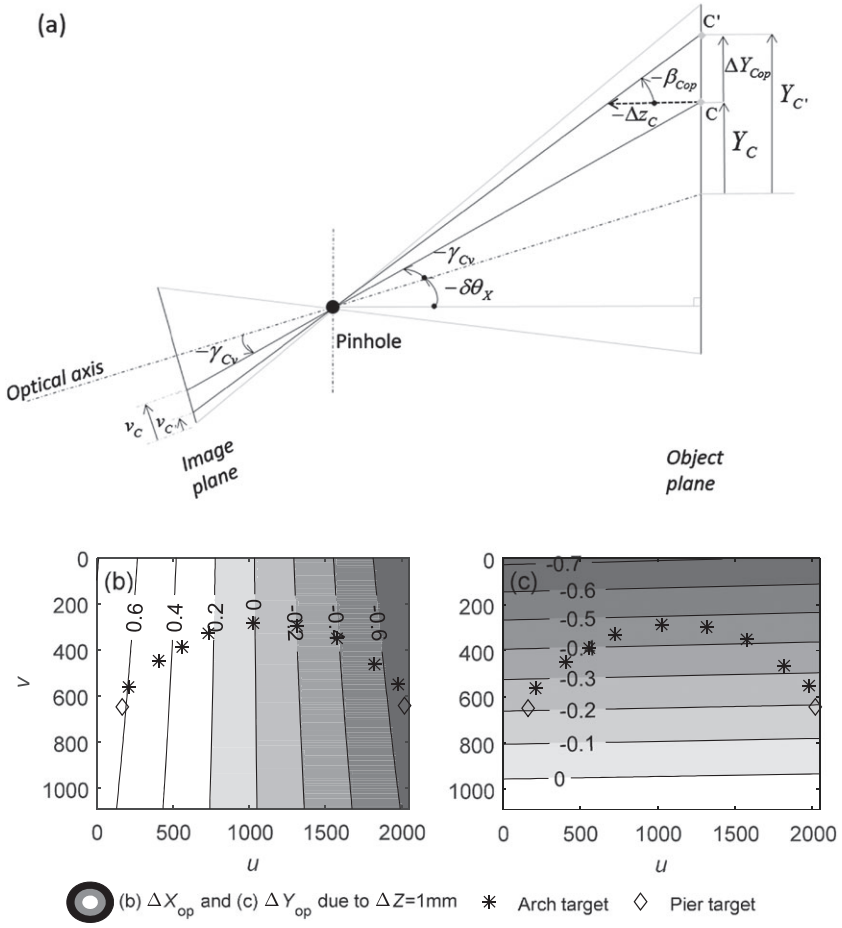

FIGURE 9 (a) A schematic of the side view of the nonperpendicular camera set-up utilised at Marsh Lane Viaduct, illustrating the influence of out-of-plane movements on in-plane measurements. (b–c) The influence of 1-mm out-of-plane movement on apparent in-plane ΔX and ΔY measurements is quantified with contour plots

movements. In addition, the nonzero pitch angle $\delta\theta_x$ can increase or decrease the influence of out-of-plane movements depending on target locations within the image frame.

Similarly, using the pinhole camera model presented in Section 2, apparent in-plane movements of an arbitrary point C due to out-of-plane movement can be calculated. To do this, the image plane position of points C and C′ is expressed using Equation (1) and is subtracted from each other. This yields

$$s_{Cop}\begin{bmatrix} u_{C'} \\ v_{C'} \\ 1 \end{bmatrix} = \mathbf{KR}\begin{bmatrix} 0 \\ 0 \\ \Delta Z_C \end{bmatrix} + s_C\begin{bmatrix} u_C \\ v_C \\ 1 \end{bmatrix}, \tag{8}$$

where s_{Cop} is the new scaling factor that is required to reconstruct the point C on the image plane after it moves in the out-of-plane direction. Equation (8) can be used to solve for $u_{C'}$ and $v_{C'}$, which denote the pixel position of point C after out-of-plane displacements. Then, the apparent displacements recorded by DIC due to the out-of-plane movement can be calculated as follows:

$$\begin{bmatrix} \Delta X_{Cop} \\ \Delta Y_{Cop} \\ 0 \end{bmatrix} = \mathbf{R}^{-1}\mathbf{K}^{-1}\left(s_{C'}\begin{bmatrix} u_{C'} \\ v_{C'} \\ 1 \end{bmatrix} - s_C\begin{bmatrix} u_C \\ v_C \\ 1 \end{bmatrix}\right), \tag{9}$$

where $s_{C'}$ is the scaling factor that is required to reconstruct the point C on the image plane, when ΔZ_C is assumed as zero. The apparent in-plane movements ΔX_{Cop} and ΔY_{Cop} due to $\Delta Z = 1$ mm of the object plane 38N for Dataset 1 is shown in Figure 9b–c. These contour plots show the expected ΔX_{Cop} and ΔY_{Cop} movements respectively for different locations on the image plane. Also plotted on this figure are the pixel locations of DIC targets on the arch and piers for Dataset 1. The apparent in-plane movement estimations in Figure 9b–c are in excellent agreement with Equations (6)

and (7). For instance, according to Equation (7), ΔX_{op} movement due to a 1-mm out-of-plane displacement is 0.58 mm at A1 and −0.02 mm at A5. This is in perfect agreement with the plots in Figure 9c. It clearly demonstrates that the out-of-plane movements have negligible influence on the X displacements located on the vertical centreline of the image (i.e., around A5), and their influence at the edges of the image is significant (i.e., around A1). Similarly, the estimated ΔY_{op} movement due to a 1-mm out-of-plane displacement can be calculated as −0.26 mm at A1 and −0.48 mm at A5 using Equation (6) ($\delta\theta_X = -15.3^{\circ}$ according to Table 2). Figure 9c validates these results. In this case, the horizontal image centreline passes near targets A1–A9. However, due to the nonzero pitch angle, the out-of-plane movements affect the in-plane measurements even in the centre of the image. For this particular camera and target arrangement, the pitch angle increases the influence of out-of-plane movements on apparent Δy movements, particularly at the top of the image.

Figure 9 indicates that small out-of-plane displacements can cause relatively large apparent in-plane displacements. Therefore, the influence of out-of-plane movement related measurement errors can be significant on absolute and relative displacement accuracy. However, different out-of-plane movements may be observed at each monitoring target. Therefore, a systematic method is necessary to deduce the out-of-plane movements and remove their influence on the data. In order to do this, Figure 10 compares the FBG and DIC relative displacement measurements between consecutive monitoring targets A1–A5. The DIC system computes the relative displacements by finding the component of axial displacement between two targets along their initial direction angle α_{gage}. For the FBG system, the relative axial displacements are determined by multiplying strain with the axial length L_{gage} between monitoring targets. L_{gage} and α_{gage} are determined from pixel position of targets and the calibrated extrinsic parameters, using Equation (2).

First, the relative displacements between targets A4 and A5 measured by FBG and DIC systems for Dataset 1 are examined (see Figure 10a). Although these measurements have a similar trace, the DIC data overestimate relative displacement magnitudes. The discrepancy between the two measurements can be attributed to the out-of-plane movements, which cause the consistent overestimation of relative displacement magnitudes. Yet it is not straightforward to determine the out-of-plane movement of both A4 and A5, as an infinite number of out-of-plane displacements can cause the discrepancy observed in Figure 10a. At this stage, it is useful to note that the targets A4 and A5 are located at the crown area of the arch, which can be assumed to be flat, for example, $\alpha_{gage} = 0.15 \approx 0$. Therefore, only relative displacements between A4 and A5 in the direction of X and caused by out-of-plane movements can lead to the systematic errors observed in Figure 10a. According to Figure 9b, any out-of-plane movement of A5 is expected to cause negligible movement in the direction of X, as this target lies close to the image vertical centreline. Therefore, the errors in the relative displacements in Figure 10a may be attributed entirely to the out-of-plane movement experienced in A4.

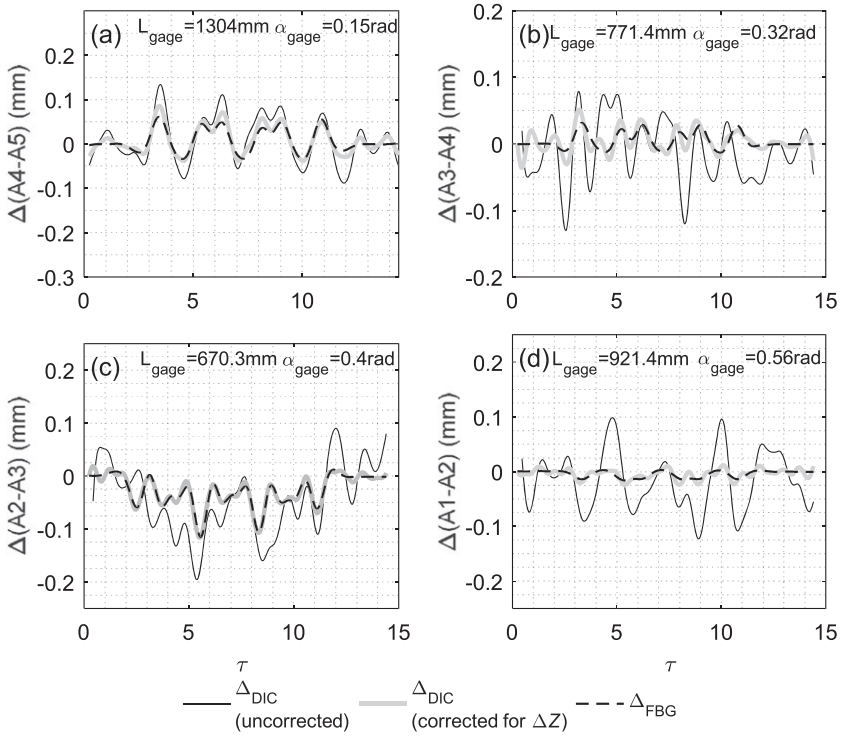

FIGURE 10 Four consecutive relative displacement measurements on the arch barrel from Dataset 1 by using digital image correlation (DIC) and fibre Bragg grating (FBG) techniques

Using this information, the out-of-plane movement of A4 can be calculated precisely. After correcting the influence of out-of-plane movements at A4, a very good agreement can be achieved between the relative displacement data between the FBG and DIC datasets of A4 and A5, which is plotted also in Figure 10a.

Following this, the relative displacement signal between monitoring targets A3 and A4 can be examined (see Figure 10b). By calculating the discrepancy between the DIC and FBG measurements, the out-of-plane movements at A3 can be estimated, and the data can be corrected for removing its influence. If this process is repeated for the consecutive targets, the out-of-plane influence for targets A1–A4 can be calculated and removed one by one. A similar process may be repeated for the targets A6–A9 to remove the out-of-plane influence on the east side of the arch.

The abovementioned procedure is illustrated as an algorithm in Figure 11. This algorithm determines the out-of-plane movement for monitoring targets A4–A1 and A6–A9 one by one, while removing the influence of out-of-plane movements on the data. In addition, to determine the out-of-plane movement at the crown target A5, the algorithm averages the determined out-of-plane movement at the targets A4 and A6. This allows estimation of the approximate out-of-plane movement at A5 and correcting for this influence. Note that the correction for out-of-plane movement at A5 does not impact the corrected relative displacements A4–A5 and A5–A6 significantly. Similarly, to determine the out-of-plane movement at the WP and EP pier targets, another approximation is necessary. Due to their proximity to targets A1 and A9, the out-of-plane movement at WP and EP pier targets is assumed to be identical to those at A1 and A9, although this is likely to be an overestimation. The influence of out-of-plane movements at WP and EP is then removed.

Figure 12 shows the corrected relative displacement time histories for several monitoring targets, alongside the calculated out-of-plane displacements (Dataset 1). Figure 12a shows the horizontal displacement $\Delta X(A5 - A1)$ before and after correction for the influence of out-of-plane movements. In particular, ΔZ_{A1} affects this trace. At the instant of $\tau = 3.5$, an out-of-plane movement of 0.3 mm was observed at A1. This influenced the horizontal displacement measurements $\Delta X(A5 - A1)$ and increased the correct measurement of −0.53 by 0.2 mm. At the next highlighted instant of $\tau = 4.5$, the out-of-plane displacement was −0.2 mm. This caused a decrease in the actual measurement by 0.09 mm. In general, correcting for the out-of-plane movements resulted in a notable increase of the magnitude of displacements for the monitoring target A1 horizontal displacements and resulted in a more orderly and physically meaningful trace. Figure 12b shows similar results for the relative vertical displacement data of the monitoring target A5 at the crown and A1 at the springing. Out-of-plane movements are notably small at the crown, and correcting the out-of-plane influence causes the magnitude of relative vertical displacements to slightly increase.

The calculated out-of-plane movements for Dataset 1 demonstrate interesting transverse response mechanisms of the bridge. For instance, when the leading axle is above the crown of 38N at $\tau = 3.5$, targets A1 and A9 move towards the spandrel wall by approximately 0.3 mm (see Figure 12c). In the meanwhile, the crown of the arch moves slightly towards the camera, in the negative Z direction by less than 0.1 mm. The pronounced positive out-of-plane movement of targets A1 and A9 indicates spreading of the relieving arch and potential opening of the longitudinal crack when the train axles are above Arch 38 (see Figure 3 and the discussion in Section 3). Finally, Figure 12d plots the span opening and closing trace ΔWP – EP after the correction of out-of-plane movements. Comparing the out-of-plane corrected DIC measurement with the uncorrected measurement and the FBG data, it is clear that the compensation for the out-of-plane movements increases the span opening estimations, whereas the span closing estimations do not change significantly. This is useful, as the uncorrected ΔWP – EP signal underestimates span opening. However, likely due to the

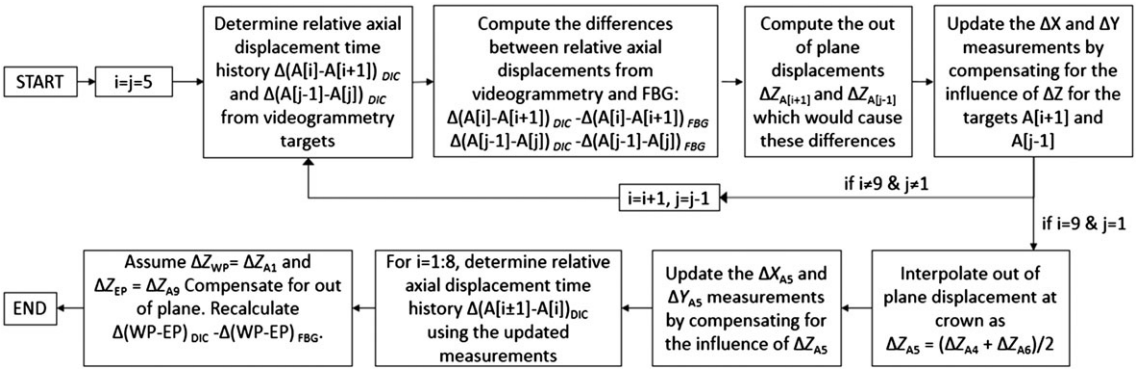

FIGURE 11 A block diagram that explains the postprocessing algorithm developed to determine the out-of-plane displacements and compensating for their influence in digital image correlation (DIC) data

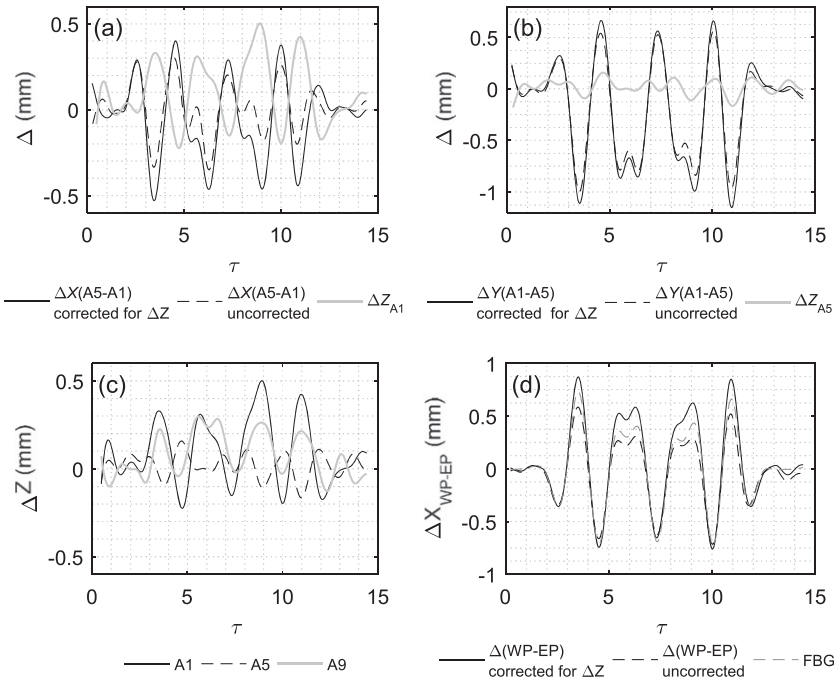

FIGURE 12 In-plane relative displacement time histories from digital image correlation Dataset 1 before and after out-of-plane correction: (a) relative horizontal displacement between A1 and A5 plotted with the out-of-plane displacement at A1 and (b) relative vertical displacement between A1 and A5 plotted with the out-of-plane displacement at A5 and (d) relative displacement between WP and EP. The out-of-plane displacement time histories for monitoring targets (c) A1, A5, and A9 are also plotted

assumption of identical out-of-plane movement at WP and EP pier targets and those at A1 and A9 (see Figure 11), the magnitude of out-of-plane correction is not accurate for ΔWP – EP.

Figure 13 demonstrates the results obtained using the proposed algorithm for five similar trains (Datasets 1–5). In particular, the out-of-plane movements at A1 and A5 are reported in Figure 13a,c. These out-of-plane signals demonstrate similar trends to those discussed earlier; for all five datasets, the out-of-plane movements at A1 are larger in magnitude compared with out-of-plane movements at A5. Although the calculated out-of-plane data from five datasets demonstrate similar traces, significant measurement noise exists. This noise is due to the out-of-plane correction algorithm (Figure 11), which assumes that all discrepancies between the FBG and DIC datasets are due to out-of-plane errors. This assumption leads to erroneous amplification of errors from other sources (e.g., lighting changes) when calculating the out-of-plane component. Δ*X*(A5 – A1) and Δ*Y*(A1 – A5) data in Figure 13b,d show the relative displacements after out-of-plane corrections are done. The repeatability of these signals is evaluated using the variation of

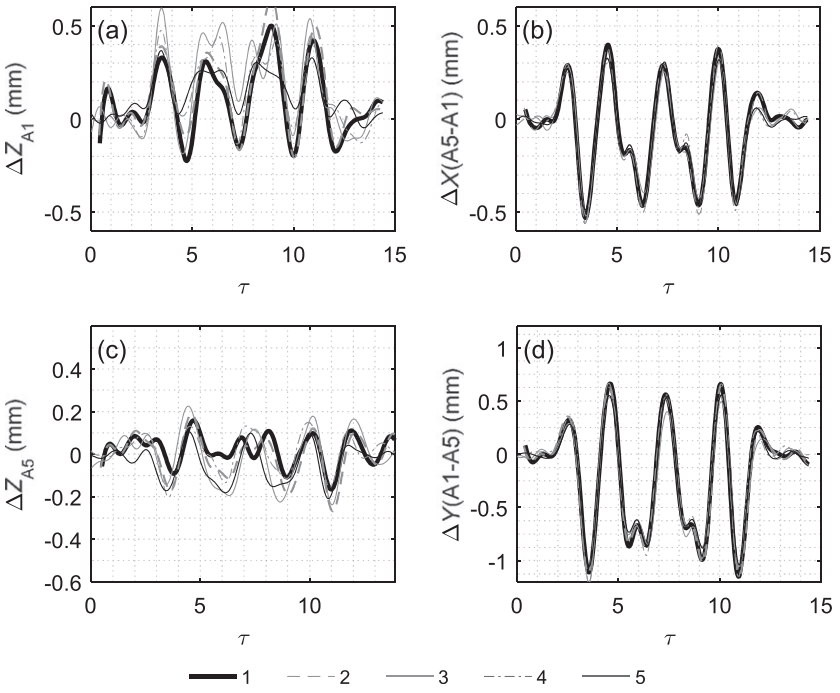

FIGURE 13 Displacement time histories from digital image correlation Datasets 1–5: (a,c) transverse displacement at 38N springing and crown and (b,d) relative horizontal and vertical displacements between the crown and springing point, which have been corrected for out-of-plane movements

the peak value of the in-plane displacement signal at specific instances, as in Section 5. Around the instance of $\tau = 3.5$, a repeatability of approximately 0.03 and 0.06 mm, respectively, was observed for the corrected datasets presented in Figure 11. This suggests that the out-of-plane correction did not adversely influence the repeatability of the data, with reference to the uncorrected data in Table 4 (which ranged from 0.02 to 0.09 mm for other relative displacement signals).

It is important to note that the out-of-plane correction technique presented herein benefitted from the combined use of the FBG and DIC monitoring techniques. Through the FBG strain data, DIC measurements were corrected, and consistent 3D displacement data from the viaduct were obtained. More generally, the quantification of out-of-plane errors presented in this section with simple geometry and pinhole camera models provides useful information on the potential impact of out-of-plane movements on DIC in-plane measurements. These findings can be used to minimise out-of-plane movement related errors during equipment set-up in future installations or provide the analytical basis for calculation of errors when additional out-of-plane measurements are available. Nonetheless, the results clearly demonstrate the need to evaluate out-of-plane measurements with supplementary out-of-plane movement measurements (e.g., indirectly via FBGs or directly with a laser vibrometer) when 2D DIC is utilised for monitoring masonry arch bridges. If it is known ahead of monitoring that out-of-plane movements are likely to be significant, it may be more suitable to use the 3D DIC technique with a stereoscopic camera set-up.[38]

7 | CONCLUSIONS

Inspired by the ability of commercial DIC systems to provide noncontact, precise, and multipoint displacement measurements, this paper investigated the dynamic displacement measurement of a masonry viaduct using Imetrum's DMS system. In order to achieve high measurement accuracies, potential sources of errors that can influence field measurements were initially surveyed. Based on previously published literature, this survey outlined the significance of errors due to equipment set-up, lighting effects, target quality, camera movements, and metric calibration. Methods to mitigate these errors during equipment set-up and data processing were discussed. In particular, a method to calibrate data using vanishing points and a single distance in the image was proposed for multipoint displacement measurement. This calibration method is more efficient than the full registration method and requires similar amount of information to the simple scaling factor method.

With a wide field of view camera configuration, the DIC system allowed noncontact and precise measurement of many displacement targets, distributed around an arch of the Marsh Lane Viaduct. Measuring relative displacement between targets on piers allowed direct measurement of span opening and closing, which provides a useful quantification of the magnitude of dynamic response. In addition, measuring relative displacement between consecutive targets on the arch allowed measurement of crown vertical deflection and strains. By using the dynamic response data from different trains (which was demonstrated to be quasistatic) and different monitoring systems (2D DIC and FBG systems), the resolution, repeatability, and accuracy of the DIC system were determined. As expected, the DIC system achieved a resolution and repeatability close to 0.1 mm for relative displacements.

A direct comparison of the DIC data to the more precise FBG data revealed systematic errors in measurements, which were investigated in detail. To identify the sources of these errors, the influence of radial distortions and out-of-plane movements on relative displacement measurements was theoretically investigated with division and pinhole camera models. After identifying the significant potential of out-of-plane movements to cause the observed errors, a new algorithm was proposed that uses the discrepancies between DIC and FBG data to estimate out-of-plane movements and correct for their influence. Consistent 3D displacement data were obtained after these corrections, which indicated a complex but repeatable and physically meaningful 3D behaviour of the viaduct.

ACKNOWLEDGEMENTS

The work carried out was funded by EPSRC and Innovate UK, through the Cambridge Centre for Smart Infrastructure and Construction (Grant EP/L010917/1). The research materials supporting this publication can be accessed at https://doi.org/10.17863/CAM.21867. The authors would like to thank Mark Norman of Network Rail and Mungo Morgan and Simon Jenkins of Imetrum for their support. They would additionally like to thank Jason Shardelow, Melanie Banes, Giuseppe Narciso, and Mehdi Alhaddad for their assistance in data collection and interpretation. The useful comments of anonymous reviewers helped improve the manuscript and are gratefully acknowledged.

ORCID

Sinan Acikgoz http://orcid.org/0000-0002-3901-574X

REFERENCES

[1] Z. Orban, Assessment, Reliability and Maintenance of Masonry, in *Arch Bridges IV-Advances in Assessment, Structural Design and Construction*, (Eds: P. Roca, C. Molins), CIMNE, Barcelona **2004**.

[2] L. D. McKibbins, C. Melbourne, N. Sawar, C. S. Gaillard, *CIRIA C656: Masonry arch bridges: condition appraisal and remedial treatment*, CIRIA, London **2006**.

[3] UIC Masonry Arch Bridges Study Group, *Assessment, Reliability and Maintenance of Masonry Arch Bridges, State-of-the-Art Research Report*, International Union of Railways, Paris **2004**.

[4] Network Rail, *NR/GN/CIV/025: The Structural Assessment of Underbridges*, Network Rail, London **2006**.

[5] Network Rail, Part Detailed Examination Report of Arch 37, Marsh Lane Viaduct **2005**.

[6] Network Rail, Part Detailed Examination Report of Arch 38, Marsh Lane Viaduct **2005**.

[7] N. Gibbons, *Modelling and Assessment of Masonry Arch Bridges*, University College Dublin, Ireland **2014**.

[8] C. Brookes, Pop bottle bridge supplementary load test. Southampton, UK: **2004**.

[9] R. Helmerich, E. Niederleithinger, C. Trela, J. Bień, T. Kamiński, *Struct. Infrastruct. Eng.* **2012**, *8*(1), 27.

[10] H. H. Nassif, M. Gindy, J. Davis, *NDT&E Int.* **2005**, *38*(3), 213.

[11] C. Gentile, G. Bernardini, *Struct. Infrastruct. Eng.* **2010**, *6*(5), 521.

[12] B. Pan, K. Qian, H. Xie, A. Asundi, *Meas. Sci. Technol.* **2009**, *20*, 1.

[13] J. Lord, N. McCormick, *Proc. ICE Civil Eng.* **2012**, *165*(4), 185.

[14] D. J. White, W. A. Take, M. D. Bolton, *Geotechnique* **2003**, *53*(7), 619.

[15] G. A. Stephen, J. M. W. Brownjohn, C. A. Taylor, *Eng. Struct.* **1993**, *15*(3), 197.

[16] J. J. Lee, M. Shinozuka, *Exp. Mech.* **2006**, *46*, 105.

[17] S. Yoneyama, H. Ueda, *Mater. Trans.* **2012**, *53*(2), 285.

[18] M. Alhaddad, Photogrammetric monitoring of cast-iron tunnels and applicabilty of empirical methods for damage assessment. University of Cambridge, **2016**.

[19] A. Hoag, A. Take, N. Hoult, C. River, *in Proceedings of the ICE Bridge Eng.* **2017**, *170*(BE3), 168.

[20] L. Tian, B. Pan, *Sensors* **2016**, *16*(9), 1.

[21] C. A. Murray, W. A. Take, N. A. Hoult, *Int. J. Phys. Model. Geotechnics* **2017**, *17*(1), 41.

[22] T. Khuc, N. Catbas, *Struct. Control Health Monit.* **2017**, *24*, 1. https://doi.org/10.1002/stc

[23] R. Hartley, A. Zisserman, *Multiple View Geometry in Computer Vision*, Cambridge University Press, Cambridge **2003**.

[24] E. Guillou, D. Meneveaux, E. Maisel, K. Bouatouch, *Vis. Comput.* **2000**, *16*, 396.

[25] R. Orghidan, J. Salvi, M. Gordan, B. Orza, *in Proceedings of the* Federated Conference on Computer Science and Information Systems, Wroclaw: **2012**.

[26] B. Pan, D. Wu, Y. Xia, *Opt. Laser Technol.* **2012**, *44*(1), 204. https://doi.org/10.1016/j.optlastec.2011.06.019

[27] G. Busca, A. Cigada, P. Mazzoleni, E. Zappa, *Exp. Mech.* **2014**, *54*, 255.

[28] B. Pan, L. Yu, D. Wu, L. Tang, *Opt. Lasers Eng.* **2013**, *51*(2), 140.

[29] Y. Xu, J. M. W. Brownjohn, *J. Civil Struct. Health Monit.* **2017**, *8*, 91. https://doi.org/10.1007/s13349-017-0261-4

[30] A. Fitzgibbon, in *Proc. of the IEEE Conference on Computer Vision and Pattern Recognition* **2001**, *1*, I-125-I-132.

[31] R. Strand, E. Hayman, in *Proc. of the British Machine Vision Conference* **2005**. https://doi.org/10.5244/C.19.9

[32] J. M. W. Brownjohn, Y. Xu, D. Hester, *Front. Built Environ.* **2017**, *3*, 1.

[33] M. Q. Feng, Y. Fukuda, D. Feng, M. Mizuta, *J. Bridge Eng.* **2015**, *20*(12), 1.

[34] J. G. Chen, N. Wadhwa, Y. J. Cha, F. Durand, W. T. Freeman, O. Buyukozturk, *J. Sound Vib.* **2015**, *345*, 58.

[35] H. Yoon, H. Elanwar, H. Choi, M. Golparvar-Fard, B. F. Spencer, *Struct. Control Health Monit.* **2016**, *23*, 1405.

[36] B. Pan, Z. Lu, H. Xie, *Opt. Lasers Eng.* **2010**, *48*(4), 469.

[37] P. W. Waterfall, M. C. Read-Jennings, F. Scenini, N. McCormick, presented at *The Ninth International Conf. on Condition Monitoring and Machinery Failure Prevention Technologies*, **2012**.

[38] M. A. Sutton, J. H. Yan, V. Tiwari, H. W. Schreier, J. J. Orteu, *Opt. Lasers Eng.* **2008**, *46*(10), 746.

[39] M. Majumder, T. K. Gangopadhyay, A. K. Chakraborty, K. Dasgupta, D. K. Bhattacharya, *Sens. Actuators, A* **2008**, *147*(1), 150.

[40] S. Acikgoz, M. J. DeJong, C. Kechavarzi, K. Soga, *Eng. Struct.*, **2018**.

[41] C. Ye, S. Acikgoz, S. Pendrigh, E. Riley, M. DeJong, *Eng. Struct.*, **2018**.

How to cite this article: Acikgoz S, DeJong MJ, Soga K. Sensing dynamic displacements in masonry rail bridges using 2D digital image correlation. *Struct Control Health Monit*. 2018;e2187. https://doi.org/10.1002/stc.2187